surfaces

MDPI

Article

TPA and PET Photo-Degradation by Heterogeneous Catalysis Using a $(Al_2O_3)_{0.75}TiO_2$ Coating

Mónica A. Camacho-González [1], Alberto Hernández-Reyes [1], Aristeo Garrido-Hernández [2], Octavio Olivares-Xometl [3], Natalya V. Likhanova [4] and Irina V. Lijanova [1,*]

[1] Instituto Politécnico Nacional, Centro de Innovación e Investigación Tecnológica, Cerrada Cecati S/N, Colonia Santa Catarina de Azcapotzalco, Ciudad de Mexico 02250, Mexico; mcamachog2200@alumno.ipn.mx (M.A.C.-G.); ahernandezr2200@alumno.ipn.mx (A.H.-R.)
[2] Departamento de Materiales, Universidad Autónoma Metropolitana, Av. San Pablo 420, Col. Nueva el Rosario, Azcapotzalco, Ciudad de Mexico 02128, Mexico; agh@azc.uam.mx
[3] Facultad de Ingeniería Química, Benemérita Universidad Autónoma de Puebla, Av. San Claudio y 18 Sur, Ciudad Universitaria, Col. San Manuel, Puebla 72570, Mexico; octavio.olivares@correo.buap.mx
[4] Instituto Mexicano del Petróleo, Eje Central Norte Lázaro Cárdenas No. 152, Col. San Bartolo Atepehuacan, Del. Gustavo A. Madero, Ciudad de Mexico 07730, Mexico; nvictoro@imp.mx
* Correspondence: ivictorvnal@ipn.mx

Abstract: The combination of the catalytic properties of Al_2O_3/TiO_2 formed an efficient system to degrade the ubiquitous pollutants TPA and PET. The coating $(Al_2O_3)_{0.75}TiO_2$ was characterized by X-ray diffraction. Stainless steel disks with photo-catalyst coating were placed transversely in a 3.0 L vertical glass reactor with ascending airflow for supplying oxygen to the reaction medium and visible light lamps for photo-activation. The analysis of the coating homogeneity, morphology and particle size distribution of the TiO_2 coatings and $(Al_2O_3)_{0.75}TiO_2$ system were confirmed by SEM. Optical properties and band-gap energy were calculated by using the Tauc equation. UV–Vis spectrophotometry (UV–Vis) and chemical oxygen demand (COD) were the quantitative techniques to measure the reduction in the initial TPA and PET concentrations.

Keywords: TPA; PET; photo-degradation; heterogeneous catalysis

check for updates

Academic Editor: Aleksey Yerokhin

Received: 25 March 2025
Revised: 14 May 2025
Accepted: 16 May 2025
Published: 21 May 2025

Citation: Camacho-González, M.A.; Hernández-Reyes, A.; Garrido-Hernández, A.; Olivares-Xometl, O.; Likhanova, N.V.; Lijanova, I.V. TPA and PET Photo-Degradation by Heterogeneous Catalysis Using a $(Al_2O_3)_{0.75}TiO_2$ Coating. *Surfaces* **2025**, *8*, 34. https://doi.org/10.3390/surfaces8020034

Copyright: © 2025 by the authors. Licensee MDPI, Basel, Switzerland. This article is an open access article distributed under the terms and conditions of the Creative Commons Attribution (CC BY) license (https://creativecommons.org/licenses/by/4.0/).

1. Introduction

Polyethylene terephthalate (PET) is the most widely used thermoplastic polymer in various areas due to its application diversity, as well as to its strength, lightness, elasticity, and transparency properties [1]. In contrast, its degradation rate is low by acid or basic hydrolysis, methanolysis, glycolysis, and acetolysis, which are chemical methods that can depolymerize PET into monomers such as terephthalic acid, ethylene glycol diacetate, colorants, and special additives [1,2]. Terephthalic acid (TPA) or 1,4-benzene dicarboxylic acid is the final product of successive oxidation reactions of p-xylene, serving as a raw material in the manufacture of PET and other plastics, dyes, perfumes, pesticides, medicines, etc. [3,4]. Wastewater discharged from the production of PET and TPA has high concentrations of different carboxylic acids like para-toluic, benzoic, acetic, phthalic, isophthalic, and an excess of terephthalic acid [5]. Due to the high stability of the aromatic structure, terephthalic acid is a ubiquitous pollutant in sediments, natural waters, soils, aquatic organisms, etc. [6]; TPA resists degradation by aerobic, anaerobic, and combined biological means and electrocoagulation [5,7–9]. In addition, TPA exerts an inhibitory effect on the growth of microorganisms, drastically decreasing the biomass during the degradation processes and extending the treatment period [10]. The refining process includes a neutralization reaction

with alkalis, which produces an excessive amount of salt and substantially reduces the efficiency of or sometimes prevents anaerobic treatment [11–13].

Recently, advanced oxidation processes (AOPs) have become more common for the effective decomposition of organic matter in wastewater, including photocatalytic oxidation, ozonation, and Fenton oxidation (H_2O_2-Fe) [14–16]. AOPs proceed by generating superreactive free radicals, which oxidize organic pollutants into less harmful or short-chain structures, which could be treated by biological means [17]. It should be emphasized that the symmetrical position of substituent groups in the aromatic ring of TPA improves its structural stability, which is widely used to detect $\bullet OH^-$ radicals generated in photocatalytic processes aiming to evaluate the effectiveness of various photocatalysts [18]. The degradation of TPA, desirably, must happen by means of non-toxic solid heterogeneous photocatalysts at ambient temperature and pressure, with the removal of multiple compounds from wastewater [19,20]. Therefore, the main challenge of AOPs is the design of an ideal photocatalyst with speedy-oxidizing power under radiation, high chemical and photo stability, low cost, and high availability [21]. Environmentally friendly TiO_2 is the most promising UV-photocatalyst with wide bandgap (anatase, 3.2 eV) and acceptable recombination of photogenerated electrons. The activation of TiO_2 by visible light could be promoted by doping it with different elements such as nickel, platinum, copper, etc., and metal oxides such as ZnO, WO_3, and Al_2O_3 to generate heterostructures that function as traps for photogenerated electrons, thus reducing their recombination and shifting absorption to the visible spectrum [22–26].

The enhancement of the photocatalytic activity of mixed oxides under UV and visible radiation was shown by Al_2O_3–TiO_2 in suspension or as thin films, in comparison with austere TiO_2 without doping [27–29]. The combination of the catalytic properties of TiO_2 and the relevant mechanical resistance, high chemical and thermal stability, and adsorption capacity of Al_2O_3 gives the system potential reusability without losing efficiency to degrade pollutants [30,31]. In specialized wastewater treatment, immobilized photocatalysts could help skip the filtration step at the end of the process; however, reducing the surface/volume ratio causes slow mass transfer and less availability of catalytically active sites [32,33]. Regardless of the nature of the photocatalyst, the design of reactors for the photocatalytic degradation of organic pollutants in aqueous solution is an area in constant development [34,35]. However, there are three fundamental limitations of a photocatalytic process: (a) mass transport, (b) efficient propagation of photons to the photocatalyst, and (c) the amount of molecular oxygen dissolved in a solution [36–38].

In this study, the purpose was to evaluate the efficiency of Al_2O_3–TiO_2 photocatalyst coatings deposited on 304 stainless steel (304 SS) (Ciudad de Mexico, Mexico) perforated disks by the dip-coating technique to degrade TPA and PET by heterogeneous photocatalysis. The disks with photocatalyst coating were placed transversely in a 3.0 L vertical glass reactor with ascending air flow to supply oxygen to the reaction medium and visible light lamps for photo-activation. UV–Vis spectrophotometry and chemical oxygen demand (COD) were the quantitative techniques employed to measure the reduction in the initial TPA and PET concentrations.

2. Materials and Methods

2.1. Coating Preparation by the Sol-Gel Route

The $(Al_2O_3)_{0.75}TiO_2$ photocatalyst (molar ratio) was obtained by the sol-gel and dip-coating techniques from precursor solutions of aluminum sulfate $[Al_2(SO_4)_3]\cdot 18H_2O$ (Meyer, Ciudad de Mexico, Mexico, 98%) and titanium tert-butoxide (TBT) (Sigma Aldrich, St. Louis, MI, USA, 97%). According to the methodology of [39], a 1 M NaOH (Meyer, Ciudad de Mexico, Mexico, ≥97%) solution was added dropwise to 95 mL of a 0.1 M

$[Al_2(SO_4)_3]$ $12H_2O$ solution until reaching pH = 10; the obtained colloidal suspension was kept under stirring at 70 °C for 5 h. Afterward, the suspension was washed three times with an ethanol/water (50:50 v/v) solution to remove SO_4^{2-} ions. The wet solid was redispersed in 50 mL of ethanol (Sigma Aldrich, St. Louis, MI, USA, 99.9%); this suspension was aged for 24 h. Four hours before the end of the aging period of the aluminum suspension, 25 mL of a 0.3 M HNO_3 (Meyer, Ciudad de Mexico, Mexico, 65%) solution were added dropwise to 30 mL of a TBT/ethanol (15% v/v) solution; the suspension was stirred for 2 h to achieve the completion of the hydrolysis–condensation reaction. Hereafter, the aluminum suspension was added to the forming $[TiO(OH)_2]_n$ gel and kept under vigorous stirring until a white milky colloidal suspension appeared. Meanwhile, five circular AISI 304 SS disks with diameters of 104 mm and orifice diameters of 2 mm were washed with non-ionic detergent soap, followed by an acetone washing in a sonication bath at 400 kHz for 20 min to eliminate oil traces, and stored in isopropyl alcohol for 1 h. Subsequently, the disks were immersed in the milky colloidal suspension of aluminum–titanium hydroxides and withdrawn at 40 mm/min. After each immersion, the disks were dried at 80 °C for 1 h; in the last of the three depositions after the treatment at 80 °C, they were treated at 180 °C for 1 h and, finally, annealed at 700 °C for 5 h. Five 304 SS disks with TiO_2 coatings were obtained by the same technique without mixing with the 0.1 M $[Al_2(SO_4)_3]\cdot 12H_2O$ solution.

2.2. Structural Characterization Measurements

The structural study of the $(Al_2O_3)_{0.75}TiO_2$ photocatalyst was carried out first, with a Bruker D8 Advance diffractometer using Cu Kα radiation (1.54184 Å), room temperature, and 2θ angle ranging from 20° to 80° with 0.02 s^{-1} pulse to determine the crystallinity and crystal phase of the produced coating. The analysis of the morphology and size of the particles was performed by employing a field emission scanning electron microscope (FE-SEM) Hitachi SU5000; for the EDS analysis, a coupled Bruker Quantax XFlash 6/60 was used to investigate the compositional aspects of the coating. The optical characteristics of the $(Al_2O_3)_{0.75}TiO_2$ coating were examined by a Perkin Elmer model Lambda 35 UV–Vis spectrophotometer from 200 to 900 nm wavelength to register absorbance values of the coating scratch.

2.3. Photocatalytic Degradation

A 3 L cylindrical reactor was designed to measure all the degradation reactions. It was made of 4 mm thick low-Fe borosilicate glass, with internal diameter and height of 111.2 and 312 mm and a top lid of the same material and diameter with 4 inlets; ascending air flow and mechanical stirring were employed. Through the top central inlet, a CPVC pipe was passed, which in addition to protect the propeller rod, served as a guide for the disks with (a) TiO_2 or (b) $(Al_2O_3)_{0.75}TiO_2$ coatings (~200 cm^2 of coating area and 44 ± 5 mg of photocatalyst per substrate). Five 104 mm diameter AISI 304 SS circular disks (alternating 2-mm holes on the entire surface) with central hole diameter of 19 mm and with-coating thickness of 1.5 mm were separated from each other by 3/4 inch CPVC tubes 40 mm in length and with an alternating 15° cutting angle at their two ends with respect to the reactor transverse axis (see Figure 1a). Through one of the lid inlets, a Polypropylene (PP) pipe (Rotoplas, Ciudad de Mexico, Mexico) was introduced to take 25 mL of solution at each time interval to quantify the COD (NMX-AA-030/2-SCFI-2011) in a HACH spectrophotometer, DR2010 (HACH company, Loveland, CO, USA). Through another inlet, a probe was introduced to measure the average pH (9.5 ± 0.2) and temperature (30 ± 0.5 °C). Eight Phillips LED lamps (4 W, 400 lumens, MR16 with emission within a 410–760 nm interval with a maximum peak at around 600 nm) were placed 20 mm from the external wall reactor in pairs at 90 degrees

to the center of the reactor for visible light irradiation (see Figure 1b,c). A black box covered the reactor and lamps to avoid external radiation.

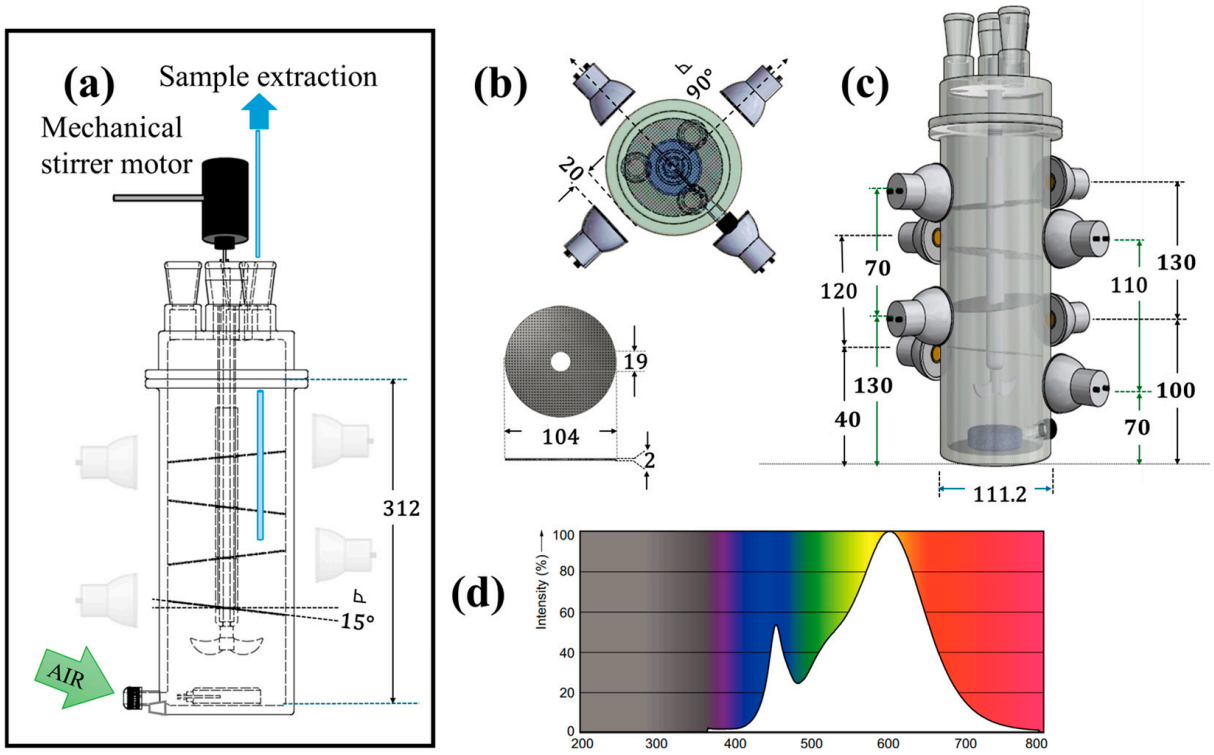


Figure 1. Airlift reactor: (**a**) arrangement of 304 SS disks with $(Al_2O_3)_{0.75}TiO_2$ coatings; (**b**) top view of the arrangement of lamps and 304 SS disks; (**c**) placement of lamps. The numbers correspond to lengths in millimeters. (**d**) Spectrum of the Philips MR16 LED lamps with color temperature of 4000 K used for the white-light optical transmission measurements.

In the reactor, 50 mg/L of TPA dissolved in 2.5 L of a 0.1% NaOH solution was homogenized by upward airflow at 5 L/min with mechanical stirring for 30 min in the absence of light to allow adsorption–desorption equilibrium between the surface of the $(Al_2O_3)_{0.75}TiO_2$ coatings and contaminant. The bubble displacement velocity by aeration-mechanical stirring was 7.26 mm/s from the time it left the diffuser to the time it left the liquid, and the flow regime was laminar (Re = 1035). The system homogeneity state was reached in 5.4 s. Subsequently, 25 mL of solution was extracted with a syringe to determine the initial TPA concentration as the COD (mg/L) immediately after the lamps were lit. Every 2 h, the same volume of solution was collected to determine the COD (mg/L). The same methodology was applied for TPA degradation with TiO_2 coatings and PET degradation using $(Al_2O_3)_{0.75}TiO_2$. Each determination was performed in triplicate. Finally, the procedure was carried out under the same conditions to degrade PET using $(Al_2O_3)_{0.75}TiO_2$. The degradation experiments were carried out in triplicate.

The efficiency of the degradation of TPA and PET was calculated with Equation (1):

$$\%degradation = \frac{COD_o - COD_t}{COD_o} \times 100 \quad (1)$$

where COD_o is the initial concentration as *COD* of each contaminant before turning on the lamps, and COD_t is the concentration of the contaminant after time t.

3. Results and Discussion

3.1. $(Al_2O_3)_{0.75}TiO_2$ Coating Characterization

3.1.1. X-Ray Diffraction

The XRD patterns of the synthesized TiO_2, Al_2O_3, and $(Al_2O_3)_{0.75}TiO_2$ oxide system powders in Figure 2 indicate that the synthesized TiO_2 exhibits predominantly the rutile phase, determined by the presence of the (110), (011), (020), (111), (120), (220), (002), (130), and (031) planes at 27.45°, 36.1°, 39.2°, 41.3°, 44.0°, 56.6°, 63°, 64.0°, and 69.06°, and 76.1°, respectively [40]. According to the ICSD chart 98-008-2085, above 500 °C, the first peak of the (110) plane, characteristic of rutile, appears at 27.5°, and near 700 °C, the anatase phase is completely transformed into rutile, being the most predominant stable phase [41].

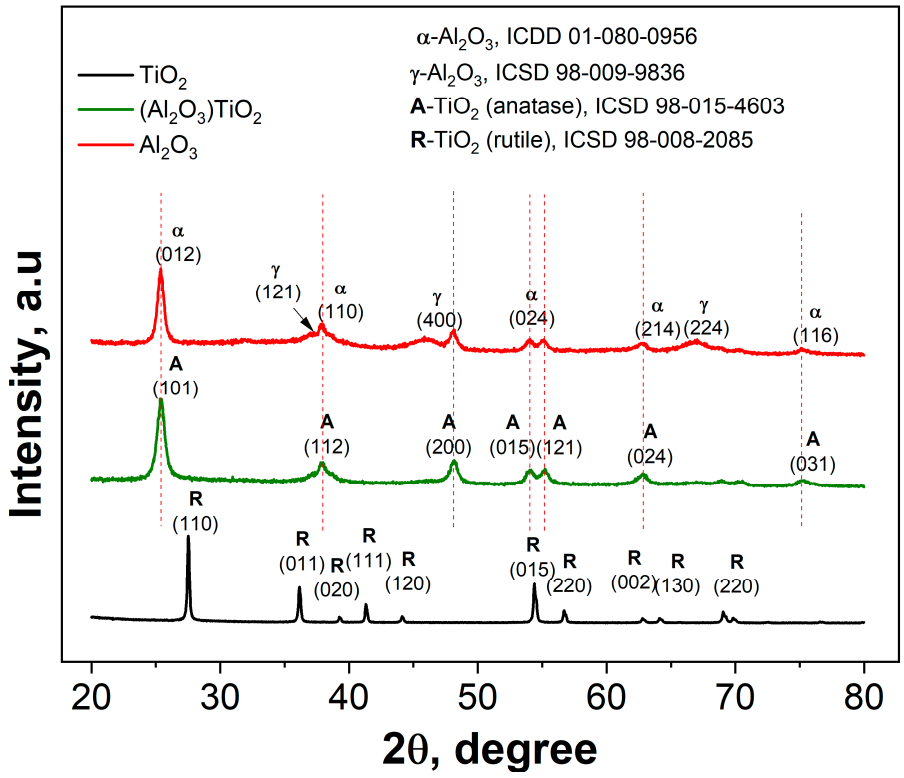


Figure 2. XRD patterns of the $(Al_2O_3)_{0.75}TiO_2$ coating powders.

In the case of the synthesized Al_2O_3, the presence of the planes (012), (110), (024), (214), and (116) is associated with the α-Al_2O_3 phase, according to the ICDD chart 01-080-0956. The γ-Al_2O_3 phase is represented by the (121), (400), and (224) planes indicated in the ICSD chart 98-009-9836. The presence of the two phases is due to the transformation of boehmite AlO(OH) into α-Al_2O_3 and even γ-Al_2O_3 was promoted by the synthesis route and heat treatment at 400–700 °C [42–44]. The presence of Al_2O_3 alters the surface energy of TiO_2, blocking the nucleation and growth of the rutile phase. This fact explains why in the $(Al_2O_3)_{0.75}TiO_2$ sample, the anatase phase has total dominance over the rutile phase according to the chart ICSD 98-015-4603, with diffraction peaks (101), (112), and (024) planes of 2θ = 25.28, 37.54, and 62.41, respectively.

The protective layers of chromium oxide and magnetite formed on the surface of 304 SS during the high-temperature treatment (near 800 °C) were detected through the structural analysis of the coating [45]. The Cr atoms could diffuse toward the grain boundaries, forming voids through which the Fe atoms in the 304 SS matrix could migrate and react with oxygen from the atmosphere or residual oxygen in the chromium-rich magnetite system: $Fe^{2+}(Fe^{3+},Cr^{3+})_2O_4$ [46,47]. Figure 3 shows the diffraction planes of stainless-steel

disks in the absence of coating, without heat treatment, and with heat treatment at 700 °C, observing this phenomenon in more detail for 5 h.

Camacho-González et al. analyzed by means of Rietveld refinement the phase composition of a 304 stainless steel substrate coated with Al_2O_3–TiO_2, synthesized under the same conditions as in this work, finding that the presence of Fe and alloying elements in the substrate was 79% of the total present phases: 72% austenite, 4% ferrite, 1% magnetite, and 2% chromium oxide, and the remaining 21% corresponded to the Al_2O_3–TiO_2 coating, where α-Al_2O_3 (7.4%) was more abundant than γ-Al_2O_3 (3%). In the case of TiO_2, the anatase phase present at 6.9% almost doubled the rutile phase with only 3.7% [39].

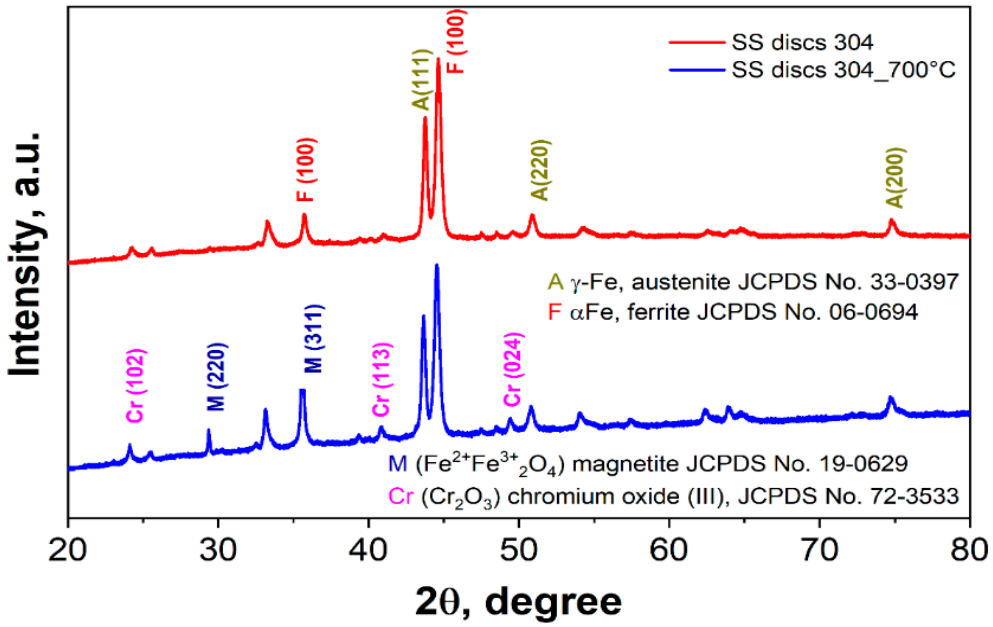


Figure 3. XRD patterns of 304 SS disks with and without thermal treatment.

3.1.2. Energy Dispersive Spectroscopy: Elemental Analysis

Figure 4 shows the micrographs and mappings of the elemental analysis of TiO_2 (area: 0.25 μm^2; magnification: 239) and $(Al_2O_3)_{0.75}TiO_2$ coating (area: 0.12 μm^2; magnification: 478) by the energy dispersive X-ray spectroscopy (EDS) technique (resolution: 512 × 444 pixels; voltage: 20.0 kV). 304 SS is composed of approximately 65–75% of Fe and alloying elements in the substrate were confirmed too: 18–20% of chromium and 8–12% of nickel, with traces of manganese (<2%), silicon (<2%), phosphorus (<0.045%), and sulfur (<0.03%), maintaining a low carbon content (<0.03%) [48]. Figure 4a shows the result of the sintering process (700 °C), where Fe (39.89%), Cr (10.4%), and Ni (3.83%) presented migration to the surface, forming the respective oxides on the TiO_2 coating surface.

Figure 4b shows the homogeneous distribution of the $(Al_2O_3)_{0.75}TiO_2$ system, confirming the presence of Al (3.83%) and Ti (2.62%) and the diffusion onto the surface of the formed Fe (32.23%) and Cr (25.15%) oxides. The constant and homogeneous distribution of oxygen in mass percentage from 22.96 to 25.46% was associated with the formation of M-O bonds between the oxygen atoms present in the coating and the surface metal atoms [49]. The molar ratio of 0.75 Al_2O_3 to 1 TiO_2 is equivalent to an atomic ratio of Al/Ti = 1.5, which is verified by the present percentage mass of these two atoms in the coating (3.83%/2.62% = 1.46).

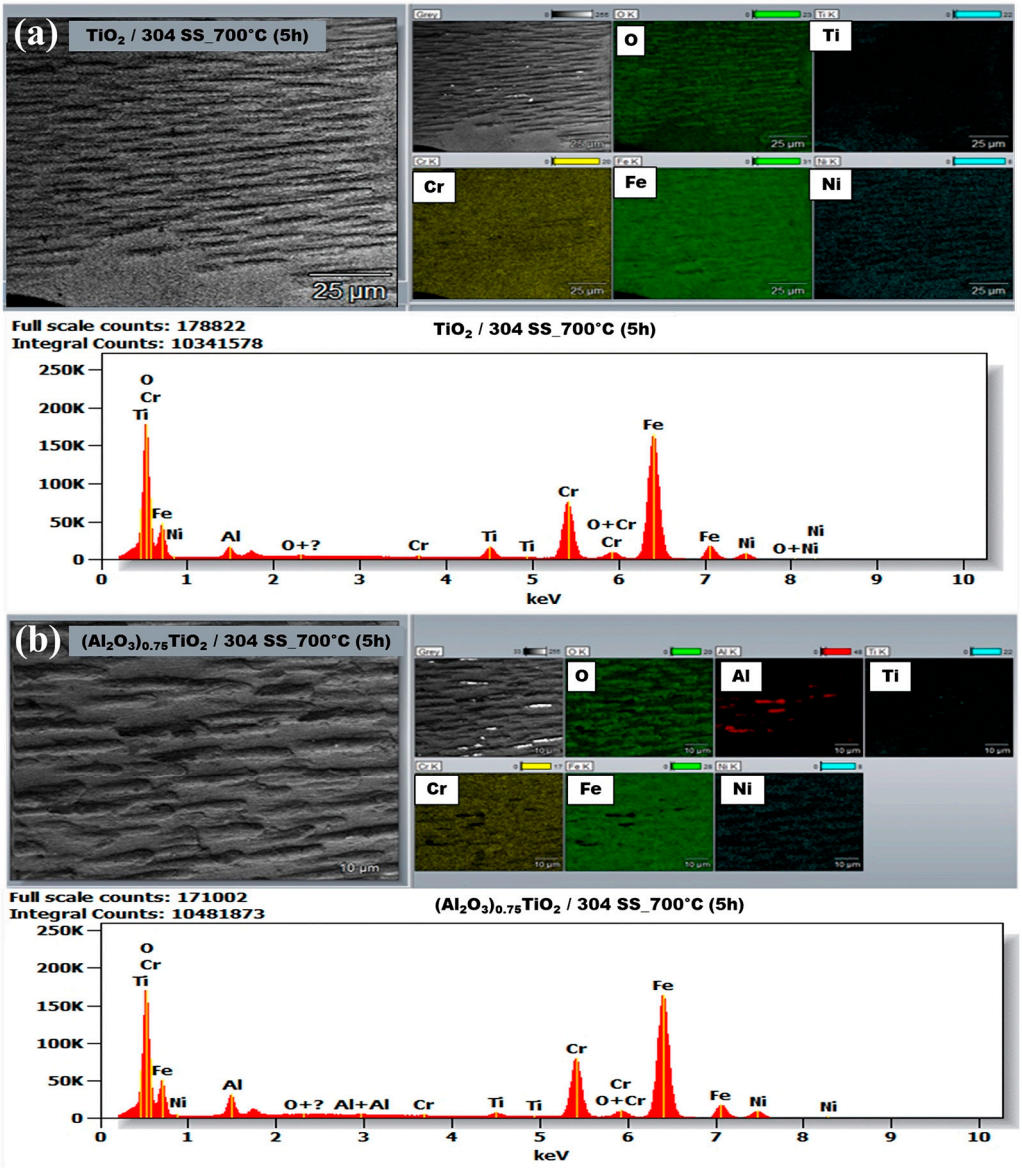


Figure 4. Micrographs and mapping of the elemental analysis of the coatings of (**a**) TiO_2 and (**b**) $(Al_2O_3)_{0.75}TiO_2$ deposited on 304 stainless steel.

3.1.3. Scanning Electron Microscopy, Morphology and Particle Size

The analysis of the coating homogeneity, morphology, and particle size distribution in the TiO_2 coatings and $(Al_2O_3)_{0.75}TiO_2$ system are shown in Figure 5; in both cases, the surface is homogeneously distributed, with no visible fractures or uncoated areas. For the TiO_2 coatings (Figure 5a) on 304 stainless steel, deposits of filamentous microstructures like rice grains are observed whose mean length distribution is 240 ± 102 nm and 54% of the measured filaments are within the interval ranging from 200 to 300 nm (Figure 5a′). Due to the independent nature of the oxides forming the system and the synthesis conditions, two different and independent morphologies are observed for the $(Al_2O_3)_{0.75}TiO_2$ coating (Figure 5b). The presence of filamentous microstructures is related to TiO_2 as previously analyzed, while the formation of spherical agglomerated particles of the $(Al_2O_3)_{0.75}TiO_2$ coating may be associated with the presence of Al_2O_3 and the sintering temperature (Figure 5b′). Liu and co-workers [50] synthesized TiO_2–SiO_2–Al_2O_3 composite coatings at different sintering temperatures on the surface of Q235 carbon steel by the sol-gel method to improve its corrosion resistance. As the authors increased the sintering temperature above 650 °C, the coating layer was composed of interlocked vine-shaped microstructures;

in addition, the appearance of porosity was observed. In the analysis, the various coating morphologies were attributed to the increase in coating components on the surface, among which, besides Al_2O_3, Fe_3O_4 and Cr_2O_3 stood out.

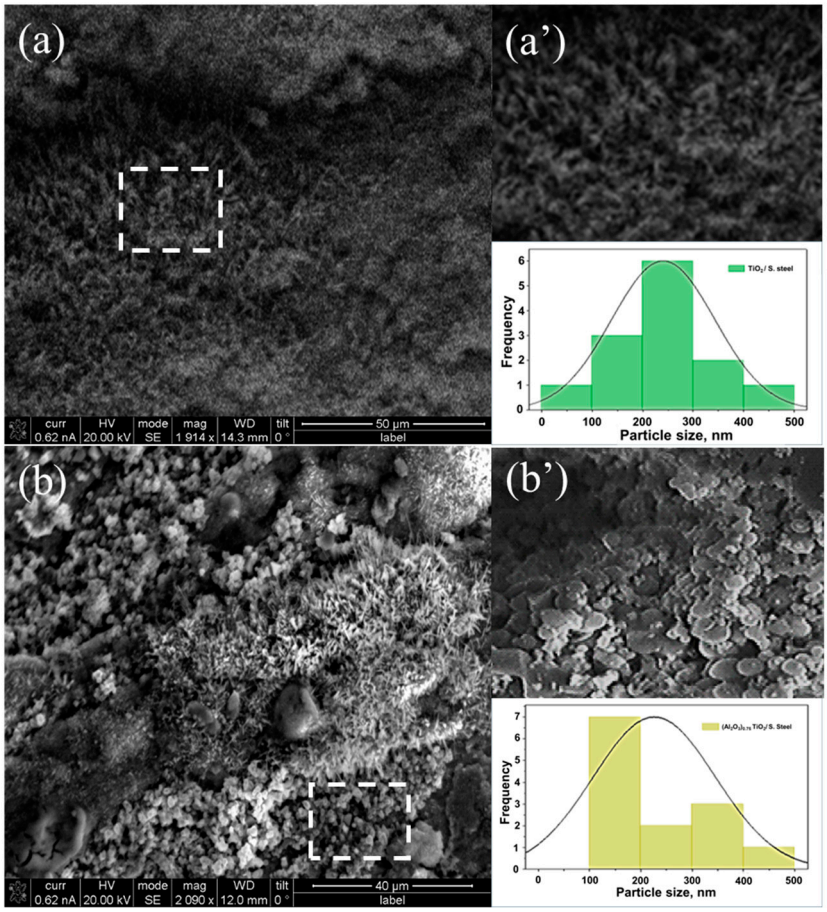


Figure 5. Micrographs of (**a**) TiO_2 coating on 304 stainless steel disks, (**a′**) magnification of the white zone of the TiO_2 coating and particle size distribution plots; (**b**) $(Al_2O_3)_{0.75}TiO_2$ coating, (**b′**) magnification of the white zone and particle size distribution plots.

The spherical particle size distribution of the $(Al_2O_3)_{0.75}TiO_2$ coating was 230 ± 120 nm. It is evident that the heterogeneity of the particles deposited on the surface allowed the formation of porosity and highly rough surfaces that could ensure a greater surface area available for the photocatalytic degradation process. In the sol-gel synthesis, during the formation of the sol, successive hydrolysis and condensation reactions gave rise to fractal aggregates, which successively joined, forming clusters whose expansion process brought the system to the solidification point or gel, changing the viscosity of the medium due to the rapid elimination of solvent. During aging, the phenomenon of syneresis (expulsion of liquid from the pores between clusters) occurred, and the successive thermal treatment caused the deformation of the polymeric network because of the loss of liquid between the pores. The increase in capillary pressure reflected the shrinkage of the network, which resulted in dense agglomerated ceramics with high porosity and high surface area, making these materials ideal catalysts and support matrices [51].

3.1.4. UV–Visible Spectroscopy: Optical Properties and Determination of the Forbidden Band Energy

The synthesis of the $(Al_2O_3)_{0.75}TiO_2$ system was conceived to have a photocatalyst whose energy absorption range in the electromagnetic spectrum shifted from the UV to

visible range, because that Al_2O_3 effectively reduces the electron–hole recombination and improves the absorption characteristics in the visible spectrum.

In Figure 6, UV–Vis spectroscopy allowed to observe two maximum absorption bands in the UV range, due to the influence of TiO_2 particles, between 220 and 230 nm and a weak absorption band between 300 nm and 350 nm. Martínez-Gómez and his team stated that these bands were the result of charge transfer from O^{2-} to Ti^{4+}, which corresponded to the excitation of electrons from the valence band of O^{2-} (2p orbitals) to the conduction band of Ti^{4+} (3d orbitals), characteristic of the anatase phase [31]. The higher visible light collection capacity between 420–625 nm of the $(Al_2O_3)_{0.75}TiO_2$ system can be related to the coating surface defects or irregularities: (a) one has a higher surface area/volume ratio, which means more active sites for photocatalytic reactions, (b) the scattering of light into multiple directions enhances the photon absorption and generation of electron-hole pairs, which are essential for photocatalytic reactions, and (c) the effective charge separation enhances the use of the photogenerated charge to degrade pollutants [52,53].

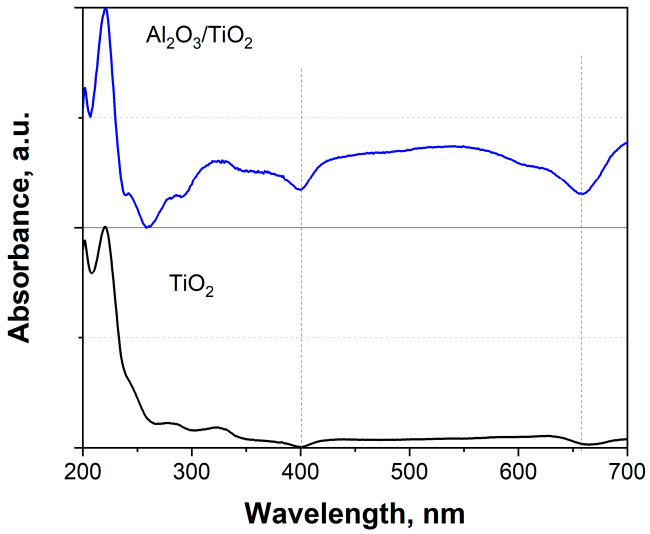


Figure 6. UV–Vis absorption spectrograms of the $(Al_2O_3)_{0.75}TiO_2$ powders.

According to Planck's equation, $E = h \cdot c / \lambda$, where E is the energy of incident radiation, h is Planck's constant (4.136×10^{-15} eV·s), c is the speed of light (2.998×10^{17} nm/s), and λ is the wavelength (nm), the energy of 5.2 eV (220 nm) relates to the modified energy levels in Al_2O_3, showing weak energy absorption below 250 nm [54]. The lifetime of charge carriers in the $(Al_2O_3)_{0.75}(TiO_2)$ system is observed by the absorption band between 300 and 380 nm [53].

The Tauc plot of the UV–Vis spectrum of the Al_2O_3–TiO_2 coating reported band gap values of 3.4 and 2.9 eV, corresponding to the anatase and rutile phases of TiO_2, respectively, and values of 4.6 and 5.2 eV for α-Al_2O_3 and γ-Al_2O_3, respectively [39]. These values are in good agreement with the data obtained from the photon energy calculated for the anatase and rutile phases of TiO_2 and alpha and gamma phases of Al_2O_3 as the interface between these oxides reported in this work.

3.2. Evaluation of the Photocatalytic Efficiency in the Degradation of Terephthalic Acid by the Immobilized $(Al_2O_3)_{0.75}TiO_2$ System

TPA exhibits characteristic absorption maxima at 190 nm, 241 nm, and 285 nm when dissolved in an acidic medium [55]. The appearance of a weak absorption band between 280 and 290 nm, which shifts to shorter wavelengths, as the polarity of the solvent increases, indicates the presence of a carbonyl group. This type of shift, called "blue shift" or

"hypsochromic", is related to the behavior of the chromophore. Likewise, an absorption band near 260 nm with fine vibrational structure is indicative of an aromatic ring [56]. Spectra in the UV region of aromatic hydrocarbons are characterized by three sets of bands originating from $\pi \rightarrow \pi^*$ transitions. Figure 7 shows the TPA spectra from 200 to 300 nm at different photocatalytic degradation breakthrough times. For TPA dissolved in 0.1% NaOH, the absorption maxima occurred at 247 nm, where the band was blue-shifted, due to the basic nature of the solution. The bands at 229 and 242 nm were assigned to the $\pi \rightarrow \pi^*$ transitions of the sp^2 C=C conjugated bonds of the aromatic ring. Likewise, at 201–202 nm, the characteristic band of the carboxyl group with $n \rightarrow \pi^*$ transition type was observed.

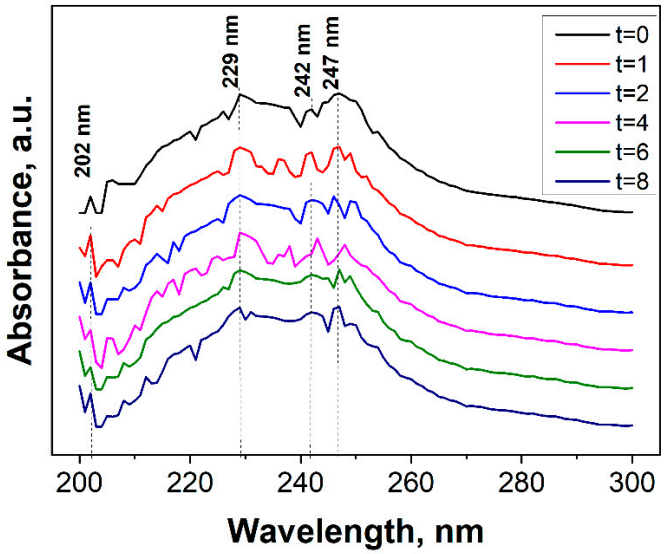


Figure 7. Monitoring of the UV–Vis absorption during the photocatalytic degradation of TPA.

As the reactions elapsed at time t, the broad band near 247 nm split into two from the first hour of reaction, which could be associated with the binding of the photogenerated OH· radical to the aromatic ring, generating 2-hydroxy-terephthalic acid (Figure 7) [57]. This reaction can be related to the attenuation of the band near 242 nm and the alternating appearance of a band around 235 nm. The band of the carboxyl group did not undergo apparent change and its conversion to CO_2 was minimal according to the 28.12% reduction in the absorbance value for this band [58]. The efficiency of photocatalytic oxidation (ZnO 2.5 g/L) of TPA reached 95%, where the operative parameters were: volume = 1.5 L, pH = 9.0, at 30 °C, adding amounts of H_2O_2 as a scavenger of photogenerated electrons to produce $OH^{\bullet}$- radicals [59]. The same studies reported that the degradation of the subsequent hydroxylation of TPA intermediates led to the cleavage of the aromatic ring, forming short-length carboxylic acids such as oxalic, formic, maleic, fumaric, and acetic that are capable of reacting directly with hydroxyl radicals, finally being mineralized to CO_2 [60].

The degradation of TPA by the action of incident light (photolysis) in the absence of disks was 4.04% and, in the presence of disks without coating, treated at 700 °C for 5 h, it was 6.22%; so, the formation of Cr_2O_3 and Fe_3O_4 by the sensitization process could promote additional TPA degradation of 1.54%. The degradation efficiency of TPA employing TiO_2 coatings on 304 SS steel disks was 28.39%, measured from the remaining concentration by absorbance at 247 nm, and this behavior was corroborated with the residual concentration measurement as COD analysis with 30.63% of degradation, observing a difference between both techniques of 1.24%, but with similar performance (Figure 8a).

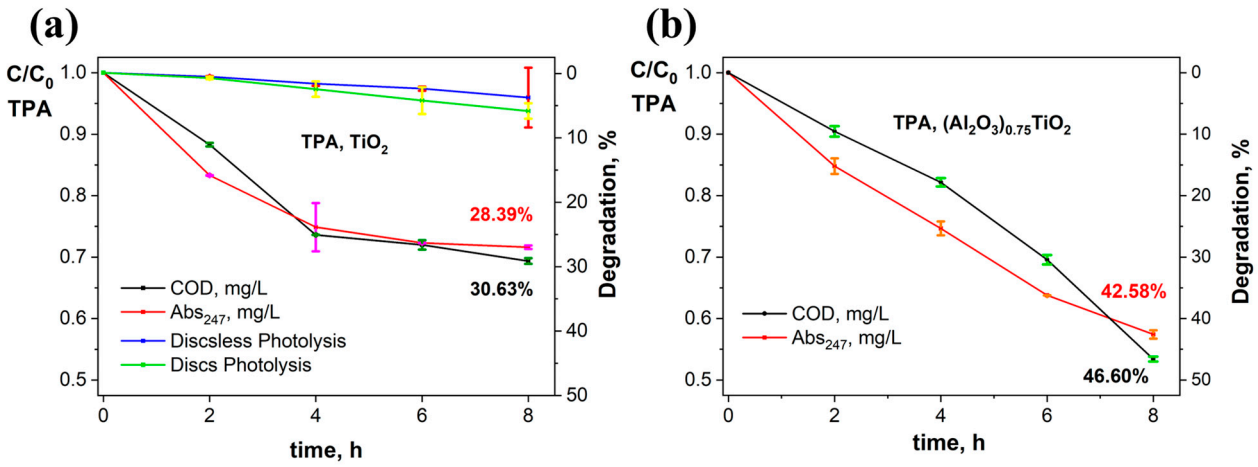


Figure 8. Photocatalytic degradation of TPA with (**a**) TiO_2 and (**b**) $(Al_2O_3)_{0.75}TiO_2$ coatings.

The degradation efficiency of TPA with $(Al_2O_3)_{0.75}TiO_2$ over 8 h, which was the duration of the reaction study, was 42.58%, measured by absorbance at 247 nm, and 46.60%, measured as COD, with a difference of 9.4% (Figure 8b).

Considering the COD measurements on TPA degradation, pseudo-first-order kinetics was observed using the Langmuir–Hinshelwood formalism as shown in the plots of ln C/Co vs. time. The apparent kinetic constants of k_{app} = 0.047 h^{-1} for TiO_2, and k_{app} = 0.0697 h^{-1} for $(Al_2O_3)_{0.75}TiO_2$ showed that the heterostructure presented higher efficiency than TiO_2 under the same operating conditions for 8 h of study (Figure 9).

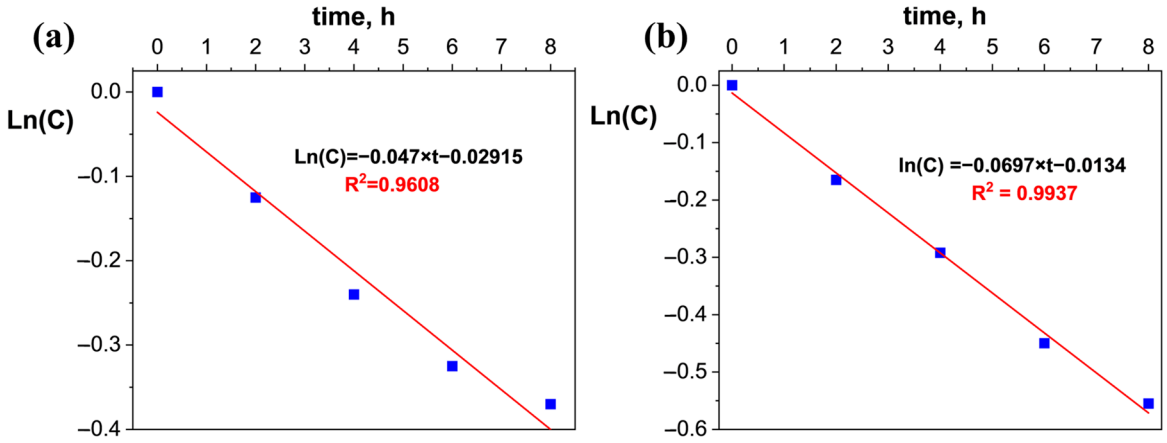


Figure 9. Photocatalytic degradation kinetics of TPA using (**a**) TiO_2, and (**b**) $(Al_2O_3)_{0.75}TiO_2$ coatings.

A band diagram for the $(Al_2O_3)_{0.75}TiO_2$ catalyst is presented in Figure 10 to understand the catalytic degradation mechanism. The synthesis methodology allowed the formation of a step-gap type heterojunction between TiO_2 and Al_2O_3, where the latter acted as an electron sink (charge carrier) that facilitated electronic transfers from anatase/rutile TiO_2 to alumina by delaying the h+-e− recombination time; the photogenerated holes on the rutile/anatase TiO_2 surface favored the formation of hydroxyl radicals by dissociation of water molecules and consequently, successive oxidation-reduction reactions could be enhanced to degrade TPA and PET into less complex organic compounds [61,62].

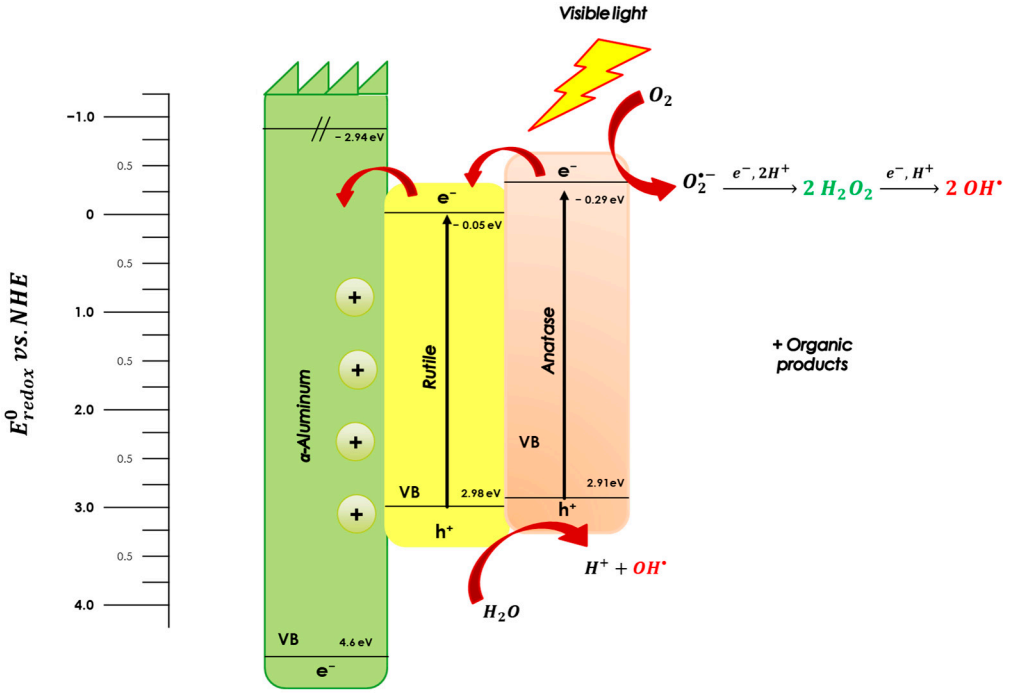


Figure 10. Band diagram for the $(Al_2O_3)0.75TiO_2$ catalyst: formation of a step-gap type heterojunction between TiO_2 and Al_2O_3.

Since TPA is a molecule that helps identify the generated OH radicals, future works will be able to verify not only the transformation of TPA into hydroxy-TPA by measuring fluorescence values during TPA degradation [18,63], but also the formation of less complex organic products using HPLC or GC-MS to validate the proposed degradation mechanism.

3.3. Evaluation of the Photocatalytic Efficiency of PET Degradation by the Immobilized $(Al_2O_3)_{0.75}TiO_2$ System

The UV–Vis spectroscopy analysis of PET shows only two broad bands at $t_0 = 0$ within the 203–207 nm interval, where the n → π* transitions of carboxyl (-COO-) and -OH-groups present in polyethylene terephthalate are commonly found (Figure 11). The other broad band between 208–213 nm is characterized by the π → π* transitions of the sp^2 C=C conjugated bonds of the aromatic ring and the bond occurring with an sp^2 carbon.

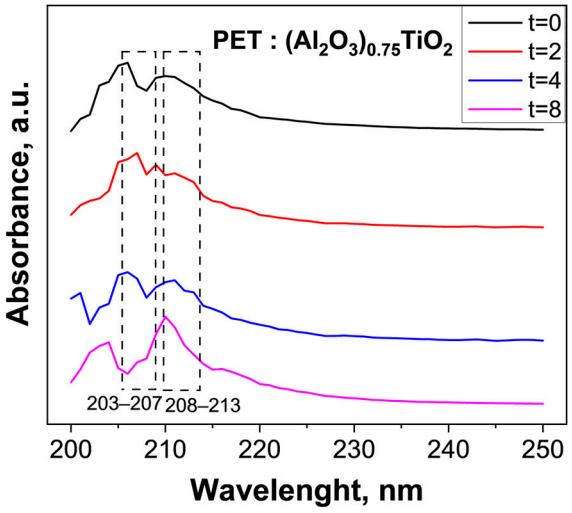


Figure 11. UV–Vis analysis of PET structural changes by heterogeneous photocatalysis by $(Al_2O_3)_{0.75}TiO_2$.

In PET, the carboxyl groups of terephthalate and OH groups of ethylene glycol are linked together by an ester bond (203–207 nm), while the repeating structural unit has, in addition to ester bonds, Csp^3-Csp^2 covalent bonds (208–213 nm). The attack of hydroxyl radicals on the ester bonds progresses the depolymerization reaction, causing the linking of the n repeating units of PET and the formation of n units of mono 2-hydroxyethyl terephthalate (MHET), and consequently PET precursors TPA and ethylene glycol. The decrease in the intensity of the absorption band of the ester bond between 203–207 nm and the appearance of the band at 201 nm, characteristic of free carboxyl groups, confirm the results [64]. The ethylene glycol molecule could be easily mineralized to CO_2 and H_2O by biological means. In addition, several studies that have addressed the microbial bioremediation of PET by various microbial consortia refer to its transformation into mono (2-hydroxyethyl) terephthalic acid (MHET) by the extracellular enzyme PETase. MHET passes to the periplasmic region of the microorganisms, where it is transformed by the enzyme MHETase into terephthalic acid and ethylene glycol [65]. Such a mechanism agrees with the analysis of the UV–Vis spectra of heterogeneous photocatalysis by the $(Al_2O_3)_{0.75}TiO_2$ system with the advantage that no strict control favoring enzymatic activity is necessary for PET biodegradation.

Figure 12 shows that the degradation efficiency of PET was 37.03%, measured by absorbance at 210 nm, and 41.18%, measured as COD; in both cases, a continuous degradation trend is observed, which could continue for more than 8 h until obtaining degradation equal to or greater than 50% of PET.

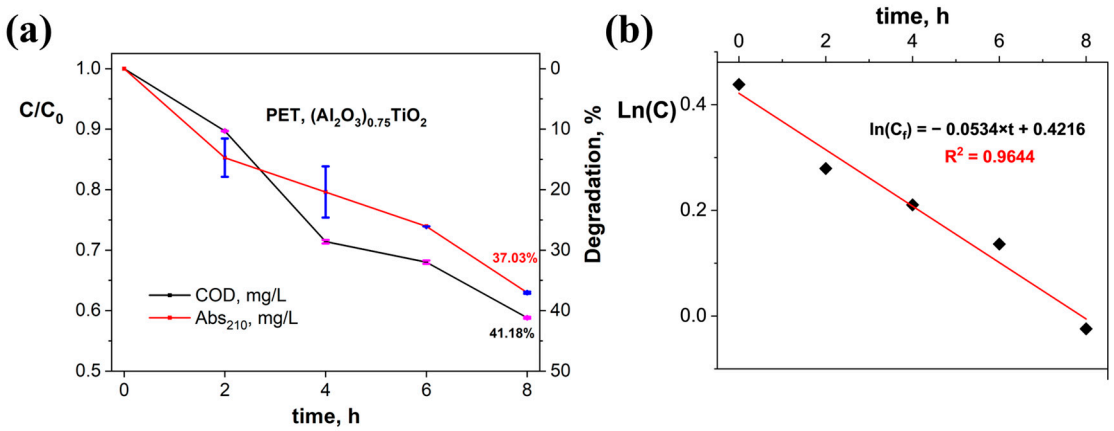


Figure 12. (**a**) Photocatalytic degradation of PET: $(Al_2O_3)_{0.75}TiO_2$ coating; (**b**) degradation kinetics.

According to the test, pseudo-first-order kinetics was observed with a photocatalysis rate constant of k_{app} = 0.0534 h^{-1}, considering the COD measurements of PET degradation. Following pseudo-first-order kinetics, 50% degradation of PET would occur in a period of approximately 13 h, which is equivalent to the half-life of the reaction (Figure 12b).

3.4. ANOVA Analysis

Analysis of variance (ANOVA) is a statistical method that was used to analyze the differences between absorbance and COD measurements performed in triplicate for each contaminant, assessing whether the group means were significantly different between them (Table 1) or not. ANOVA calculates the F value (Fischer test value) and the sum of squares to evaluate the significance of the parameters. A *p*-value less than 0.05, corresponding to a significance level of 5% or a confidence interval of 95%, indicates statistical significance.

Table 1. ANOVA analysis of triplicate experiments.

Experiment	Sum of Squares	Degree of Freedom	Mean Square	F_{value}	p_{value}	Significance
TPA_TiO_2_DQO	12,102.83	4	3025.71	3272.21	<0.05	Optimal
TPA_TiO_2_Abs_{247}	0.12	4	0.03	116.60	<0.05	Optimal
TPA_$(Al_2O_3)_{0.75}TiO_2$_DQO	25,757.96	4	6439.49	4164.36	<0.05	Optimal
TPA_$(Al_2O_3)_{0.75}TiO_2$_Abs_{247}	0.21	4	0.05	1847.31	<0.05	Optimal
PET_$(Al_2O_3)_{0.75}TiO_2$_DQO	308,610.69	4	77,152.67	22,932.53	<0.05	Optimal
PET_$(Al_2O_3)_{0.75}TiO_2$_Abs_{210}	0.35	4	0.09	126.28	<0.05	Optimal

In all the experiments, the critical F value was 3.48. Since the F values are much higher and the p values are less than 0.05, all the measurements made for each contaminant by both COD and absorbance are statistically significant, i.e., the three data sets from each experiment are different but can be considered as equivalent. These results suggest that each test, performed in triplicate, is solely dependent on the photocatalyst concentration with no other variables influencing the degradation of TPA and PET.

The highest F values were observed for the experiments that quantified the concentration by COD, indicating that this analysis is more meaningful and reproducible than the analysis by UV–Vis spectroscopy.

4. Conclusions

The selection of TPA and PET contaminants was made because TPA is the hydrolysis product of PET, PET can be degraded to TPA, and the latter can also be degraded to less toxic contaminants, which represents a challenge for water treatment technology. The reduction in the COD measurement for an initial TPA concentration of 50 mg/L in the reactor with the modified arrangement of stainless-steel disks with the $(Al_2O_3)_{0.75}TiO_2$ coating and lamps reached 46.60%. This kind of reduction could be associated with the low-scale formation of CO_2 from the TPA carboxyl groups. The UV–Vis analysis for 8 h of determination showed the splitting of initial bands, which resulted in the formation of intermediate products. Commercial PET sampling in the presence of the immobilized $(Al_2O_3)_{0.75}TiO_2$ photocatalyst reduced the COD value to 41% and the UV–Vis analysis revealed degradation efficiency of 37%.

Author Contributions: Conceptualization, I.V.L.; methodology, M.A.C.-G.; software, A.H.-R.; validation, A.G.-H.; formal analysis, N.V.L. and M.A.C.-G.; investigation, N.V.L.; resources, O.O.-X.; data curation, A.H.-R.; writing—original draft preparation, M.A.C.-G. and I.V.L.; writing—review and editing, I.V.L. and A.H.-R.; visualization, N.V.L.; supervision, A.G.-H.; project administration, M.A.C.-G.; funding acquisition, O.O.-X. All authors have read and agreed to the published version of the manuscript.

Funding: This research received no external funding.

Data Availability Statement: Data is contained within the article.

Conflicts of Interest: The authors declare no conflicts of interest.

References

1. Peng, Y.; Yang, J.; Deng, C.; Deng, J.; Shen, L.; Fu, Y. Acetolysis of waste polyethylene terephthalate for upcycling and life-cycle assessment study. *Nat. Commun.* **2023**, *14*, 3249. [CrossRef] [PubMed]
2. Fang, P.; Liu, B.; Xu, J.; Zhou, Q.; Zhang, S.; Ma, J.; Lu, X. High-efficiency glycolysis of poly(ethylene terephthalate) by sandwich-structure polyoxometalate catalyst with two active sites. *Polym. Degrad. Stab.* **2018**, *156*, 22–31. [CrossRef]
3. Xiao, Y.; Luo, W.P.; Zhang, X.Y.; Guo, C.C.; Liu, Q.; Jiang, G.F.; Li, Q.H. Aerobic Oxidation of p-Toluic Acid to Terephthalic Acid over T(p-Cl)PPMnCl/Co(OAc)2 Under Moderate Conditions. *Catal. Lett.* **2010**, *134*, 155–161. [CrossRef]

4. Zhang, H.; Wang, Y.; Li, X.; Deng, K.; Yu, H.; Xu, Y.; Wang, H.; Wang, Z.; Wang, L. Electrocatalytic upcycling of polyethylene terephthalate plastic to formic acid coupled with energy-saving hydrogen production over hierarchical Pd-doped NiTe nanoarrays. *Appl. Catal. B Environ.* **2024**, *340*, 123236. [CrossRef]
5. Ma, K.; Li, X.; Bao, L.; Li, X.; Cui, Y. The performance and bacterial community shifts in an anaerobic-aerobic process treating purified terephthalic acid wastewater under influent composition variations and ambient temperatures. *J. Clean. Prod.* **2020**, *276*, 124190. [CrossRef]
6. Billings, A.; Jones, K.C.; Pereira, M.G.; Spurgeon, D.J. Plasticisers in the terrestrial environment: Sources, occurrence and fate. *Environ. Chem.* **2021**, *18*, 111–130. [CrossRef]
7. Chang, B.V.; Yang, C.M.; Cheng, C.H.; Yuan, S.Y. Biodegradation of phthalate esters by two bacteria strains. *Chemosphere* **2004**, *55*, 533–538. [CrossRef]
8. Kleerebezem, R.; Beckers, J.; Hulshoff Pol, L.W.; Lettinga, G. High rate treatment of terephthalic acid production wastewater in a two-stage anaerobic bioreactor. *Biotechnol. Bioeng.* **2005**, *91*, 169–179. [CrossRef]
9. Sannino, D.; Vaiano, V.; Sacco, O.; Morante, N.; De Guglielmo, L.; Di Capua, G.; Femia, N. Visible Light Driven Degradation of Terephthalic Acid: Optimization of Energy Demand by Light Modulation Techniques. *J. Photocatal.* **2021**, *2*, 49–61. [CrossRef]
10. Li, H.; Zhang, W.; Xia, D.; Ye, L.; Ma, W.; Li, H.; Li, Q.; Wang, Y. Improved anaerobic degradation of purified terephthalic acid wastewater by adding nanoparticles or co-substrates to facilitate the electron transfer process. *Environ. Sci. Nano* **2022**, *9*, 1011–1024. [CrossRef]
11. Muñoz Sierra, J.D.; Lafita, C.; Gabaldón, C.; Spanjers, H.; van Lier, J.B. Trace metals supplementation in anaerobic membrane bioreactors treating highly saline phenolic wastewater. *Bioresour. Technol.* **2017**, *234*, 106–114. [CrossRef] [PubMed]
12. Zhang, H.; Wu, J.; Li, R.; Kim, D.-H.; Bi, X.; Zhang, G.; Jiang, B.; Yong Ng, H.; Shi, X. Novel intertidal wetland sediment-inoculated moving bed biofilm reactor treating high-salinity wastewater: Metagenomic sequencing revealing key functional microorganisms. *Bioresour. Technol.* **2022**, *348*, 126817. [CrossRef]
13. Ma, X.; Li, X.; Wang, X.; Liu, G.; Zuo, J.; Wang, S.; Wang, K. Impact of salinity on anaerobic microbial community structure in high organic loading purified terephthalic acid wastewater treatment system. *J. Hazard. Mater.* **2020**, *383*, 121132. [CrossRef]
14. Zhang, H.; Tian, L.; Zhang, Z.; Han, J.; Wu, Z.; Wei, Z.; Wang, S.; Cao, Y.; Zhang, S.; Zhang, Y. Effective degradation of phenol by in-situ photocatalytic-Fenton-like technology with $BiVO_4/Bi_2WO_6/Ti_3C_2$ QDs. *Surf. Interfaces* **2024**, *55*, 105315. [CrossRef]
15. Fuentes, I.; Julia, L.R.; Hugo, T.; José, M.R.-H.; Isaac, C.; Poznyak, T. Terephthalic acid decomposition by photocatalytic ozonation with VxOy/ZnO under different UV-A LEDs distributions. *Chem. Eng. Commun.* **2020**, *207*, 263–277. [CrossRef]
16. Zhu, Y.; Luo, H.; Wang, T.; Zhou, J.; Zhu, Y.; Hou, J. Advanced treatment of landfill leachate by catalytic ozonation with $MnCeOx/\gamma\text{-}Al_2O_3$ catalyst. *Surf. Interfaces* **2024**, *46*, 104113. [CrossRef]
17. Jin, Y.; Gao, Y.; Pang, D.; Li, J.; Wang, X.; Chen, G.; Wang, W.; Mao, Y. Fe3C-modified carbon composites for boosted peroxymonosulfate activation and organic pollutant decontamination: Contributions of dual radical and nonradical pathways. *Surf. Interfaces* **2024**, *46*, 104085. [CrossRef]
18. Žerjav, G.; Albreht, A.; Vovk, I.; Pintar, A. Revisiting terephthalic acid and coumarin as probes for photoluminescent determination of hydroxyl radical formation rate in heterogeneous photocatalysis. *Appl. Catal. A Gen.* **2020**, *598*, 117566. [CrossRef]
19. Sacco, O.; Vaiano, V.; Rizzo, L.; Sannino, D. Photocatalytic activity of a visible light active structured photocatalyst developed for municipal wastewater treatment. *J. Clean. Prod.* **2018**, *175*, 38–49. [CrossRef]
20. Jiang, Q.; Liu, J.; Qi, T.; Liu, Y. Enhanced visible-light photocatalytic activity and antibacterial behaviour on fluorine and graphene synergistically modified TiO_2 nanocomposite for wastewater treatment. *Environ. Technol.* **2022**, *43*, 3821–3834. [CrossRef]
21. Merino, N.; Qu, Y.; Deeb, R.A.; Hawley, E.L.; Hoffmann, M.R.; Mahendra, S. Degradation and Removal Methods for Perfluoroalkyl and Polyfluoroalkyl Substances in Water. *Environ. Eng. Sci.* **2016**, *33*, 615–649. [CrossRef]
22. Byrne, C.; Subramanian, G.; Pillai, S.C. Recent advances in photocatalysis for environmental applications. *J. Environ. Chem. Eng.* **2018**, *6*, 3531–3555. [CrossRef]
23. Al Miad, A.; Saikat, S.P.; Alam, M.K.; Sahadat Hossain, M.; Bahadur, N.M.; Ahmed, S. Metal oxide-based photocatalysts for the efficient degradation of organic pollutants for a sustainable environment: A review. *Nanoscale Adv.* **2024**, *6*, 4781–4803. [CrossRef]
24. Krishnan, A.; Swarnalal, A.; Das, D.; Krishnan, M.; Saji, V.S.; Shibli, S.M.A. A review on transition metal oxides based photocatalysts for degradation of synthetic organic pollutants. *J. Environ. Sci.* **2024**, *139*, 389–417. [CrossRef]
25. Wang, Y.; Xu, M.; Li, J.; Zhang, T. Photocatalytic Degradation of Organic Pollutants Using Al/TiO_2 Composites Under Visible Light. *Environ. Eng. Sci.* **2024**, *41*, 204–215. [CrossRef]
26. Ran, Y.; Zhong, J.; Li, J.; Li, M.; Tian, C. Substantially boosted photocatalytic detoxification activity of TiO_2 benefited from Eu doping. *Environ. Technol.* **2023**, *44*, 1313–1321. [CrossRef]
27. Zhang, Q.; Li, R.; Li, Z.; Li, A.; Wang, S.; Liang, Z.; Liao, S.; Li, C. The dependence of photocatalytic activity on the selective and nonselective deposition of noble metal cocatalysts on the facets of rutile TiO_2. *J. Catal.* **2016**, *337*, 36–44. [CrossRef]
28. Yakdoumi, F.Z.; Hadj-Hamou, A.S. Effectiveness assessment of TiO_2-Al_2O_3 nano-mixture as a filler material for improvement of packaging performance of PLA nanocomposite films. *J. Polym. Eng.* **2020**, *40*, 848–858. [CrossRef]

29. Karunakaran, C.; Magesan, P.; Gomathisankar, P.; Vinayagamoorthy, P. Absorption, emission, charge transfer resistance and photocatalytic activity of Al_2O_3/TiO_2 core/shell nanoparticles. *Superlattices Microstruct.* **2015**, *83*, 659–667. [CrossRef]
30. Magnone, E.; Kim, M.K.; Lee, H.J.; Park, J.H. Facile synthesis of TiO_2-supported Al_2O_3 ceramic hollow fiber substrates with extremely high photocatalytic activity and reusability. *Ceram. Int.* **2021**, *47*, 7764–7775. [CrossRef]
31. Martinez-Gómez, C.; Rangel-Vazquez, I.; Zarraga, R.; del Ángel, G.; Ruíz-Camacho, B.; Tzompantzi, F.; Vidal-Robles, E.; Perez-Larios, A. Photodegradation and Mineralization of Phenol Using TiO_2Coated γ-Al_2O_3: Effect of Thermic Treatment. *Processes* **2022**, *10*, 1186. [CrossRef]
32. Zhu, Y.; Ning, Y.; Li, L.; Chen, Z.; Li, H.; Zhang, Y. Effective removal of hexavalent chromium from aqueous system by biochar-supported titanium dioxide (TiO_2). *Environ. Chem.* **2022**, *19*, 432–445. [CrossRef]
33. Kanakaraju, D.; Motti, C.A.; Glass, B.D.; Oelgemöller, M. Photolysis and TiO_2-catalysed degradation of diclofenac in surface and drinking water using circulating batch photoreactors. *Environ. Chem.* **2014**, *11*, 51–62. [CrossRef]
34. Zhuang, Q.; Shi, K.; Wang, J.; Zhou, H.; Zhao, P.; Lou, Y. Revolutionizing pollution control with innovative CuO@TiO_2 nanocomposite for enhanced photocatalytic degradation and antimicrobial efficacy. *Surf. Interfaces* **2024**, *55*, 105410. [CrossRef]
35. Yu, X.; Wang, S.; Zhang, Y.; Yu, X.; Zhao, X.; Gao, H.; Yang, H.; Fang, L.; Syed, A. Biochar coupling induced charge transfer switching of a $NiAl_2O_4/NiCr_2O_4$ photocatalyst to enhance photocatalytic degradation of tetracycline hydrochloride. *Surf. Interfaces* **2024**, *54*, 105222. [CrossRef]
36. Duan, L.; Wang, B.; Heck, K.; Guo, S.; Clark, C.A.; Arredondo, J.; Wang, M.; Senftle, T.P.; Westerhoff, P.; Wen, X.; et al. Efficient Photocatalytic PFOA Degradation over Boron Nitride. *Environ. Sci. Technol. Lett.* **2020**, *7*, 613–619. [CrossRef]
37. Samy, M.; Ibrahim, M.G.; Fujii, M.; Diab, K.E.; ElKady, M.; Gar Alalm, M. CNTs/MOF-808 painted plates for extended treatment of pharmaceutical and agrochemical wastewaters in a novel photocatalytic reactor. *Chem. Eng. J.* **2021**, *406*, 127152. [CrossRef]
38. Ibarra, I.C.R.; Dubé, I.Z.; Sánchez, M.F.G. 1. MX2019002787—Reactor Fotocatalítico para la Degradación de Contaminantes Orgánicos a Presiones por Encima de los Valores Ambientales. 2019002787. 2020. Available online: https://www.wipo.int/ipcpub/?symbol=B01J0003000000&menulang=es&lang=es (accessed on 1 August 2024).
39. Camacho-González, M.A.; Lijanova, I.V.; Reyes-Miranda, J.; Sarmiento-Bustos, E.; Quezada-Cruz, M.; Vera-Serna, P.; Barrón-Meza, M.Á.; Garrido-Hernández, A. High Photocatalytic Efficiency of Al_2O_3-TiO_2 Coatings on 304 Stainless Steel for Methylene Blue and Wastewater Degradation. *Catalysts* **2023**, *13*, 1351. [CrossRef]
40. Habibi, S.; Jamshidi, M. Sol–gel synthesis of carbon-doped TiO_2 nanoparticles based on microcrystalline cellulose for efficient photocatalytic degradation of methylene blue under visible light. *Environ. Technol.* **2020**, *41*, 3233–3247. [CrossRef]
41. Farhadian Azizi, K.; Bagheri-Mohagheghi, M.-M. Transition from anatase to rutile phase in titanium dioxide (TiO_2) nanoparticles synthesized by complexing sol–gel process: Effect of kind of complexing agent and calcinating temperature. *J. Sol-Gel Sci. Technol.* **2013**, *65*, 329–335. [CrossRef]
42. Zhu, L.; Lu, Q.; Lv, L.; Wang, Y.; Hu, Y.; Deng, Z.; Lou, Z.; Hou, Y.; Teng, F. Ligand-free rutile and anatase TiO_2 nanocrystals as electron extraction layers for high performance inverted polymer solar cells. *RSC Adv.* **2017**, *7*, 20084–20092. [CrossRef]
43. Sadeq, Z.S.; Mahdi, Z.F.; Hamza, A.M. Low cost, fast and powerful performance interfacial charge transfer nanostructured Al_2O_3 capturing of light photocatalyst eco-friendly system using hydrothermal method. *Mater. Lett.* **2019**, *254*, 120–124. [CrossRef]
44. Xu, L.; Song, H.; Chou, L. Facile synthesis of nano-crystalline alpha-alumina at low temperature via an absolute ethanol sol–gel strategy. *Mater. Chem. Phys.* **2012**, *132*, 1071–1076. [CrossRef]
45. Askeland, D. *Ciencia e Ingeniería de Materiales*, 3rd ed.; Thomson, Ed.; Cengage Learning, Inc.: Toronto, ON, Canada, 2012.
46. Miglierini, M.B.; Pašteka, L.; Cesnek, M.; Kmječ, T.; Bujdoš, M.; Kohout, J. Influence of surface treatment on microstructure of stainless steels studied by Mössbauer spectrometry. *J. Radioanal. Nucl. Chem.* **2019**, *322*, 1495–1503. [CrossRef]
47. Zhang, X.; Yang, S.; Li, J.; Wu, J. Temperature-dependent evolution of oxide inclusions during heat treatment of stainless steel with yttrium addition. *Int. J. Miner. Metall. Mater.* **2020**, *27*, 754–763. [CrossRef]
48. da Trindade, C.d.M.; da Silva, S.W.; Bortolozzi, J.P.; Banús, E.D.; Bernardes, A.M.; Ulla, M.A. Synthesis and characterization of TiO_2 films onto AISI 304 metallic meshes and their application in the decomposition of the endocrine-disrupting alkylphenolic chemicals. *Appl. Surf. Sci.* **2018**, *457*, 644–654. [CrossRef]
49. Oladijo, O.P.; Popoola, A.P.I.; Booi, M.; Fayomi, J.; Collieus, L.L. Corrosion and mechanical behaviour of Al_2O_3.TiO_2 composites produced by spark plasma sintering. *South Afr. J. Chem. Eng.* **2020**, *33*, 58–66. [CrossRef]
50. Liu, X.; Wan, Y.; Zhang, X. Preparation and Corrosion Properties of TiO_2-SiO_2-Al_2O_3 Composite Coating on Q235 Carbon Steel. *Coatings* **2023**, *13*, 1994. [CrossRef]
51. Brinker, C.J.; Scherer, G.W. *Sol-Gel Science: The Physics and Chemistry of Sol-Gel Processing*; Academic Press: Cambridge, MA, USA, 2013; ISBN 0080571034.
52. Tiss, B.; Zayoud, W.; Sekrafi, H.E.; Bouguila, N.; Cristea, D.; Croitoru, C.; Velicu, L.; Tiron, V.; Prepelita, P.; Craciun, V.; et al. Enhancing photocatalysis through annealing: Unveiling the role of physical properties in photocatalytic behavior. *Mater. Chem. Phys.* **2024**, *313*, 128665. [CrossRef]

53. Ahmad, I.; Zou, Y.; Yan, J.; Liu, Y.; Shukrullah, S.; Naz, M.Y.; Hussain, H.; Khan, W.Q.; Khalid, N.R. Semiconductor photocatalysts: A critical review highlighting the various strategies to boost the photocatalytic performances for diverse applications. *Adv. Colloid Interface Sci.* **2023**, *311*, 102830. [CrossRef]
54. Akkaya Arıer, U.O.; Tepehan, F.Z. Influence of Al_2O_3:TiO_2 ratio on the structural and optical properties of TiO_2–Al_2O_3 nanocomposite films produced by sol gel method. *Compos. Part B Eng.* **2014**, *58*, 147–151. [CrossRef]
55. Kolesnik, O. UV-Vis Spectrum of Terephthalic Acid. SIELC Technol. Available online: https://sielc.com/uv-vis-spectrum-of-terephthalic-acid (accessed on 1 August 2024).
56. Skoog, D.A.; Holler, F.J.; Crouch, S.R. *Principles of Instrumental Analysis*. Cengage Learning. 2017. Available online: https://books.google.com.mx/books?id=D13EDQAAQBAJ (accessed on 1 August 2024).
57. Zielińska-Jurek, A.; Wysocka, I.; Janczarek, M.; Stampor, W.; Hupka, J. Preparation and characterization of Pt–N/TiO2 photocatalysts and their efficiency in degradation of recalcitrant chemicals. *Sep. Purif. Technol.* **2015**, *156*, 369–378. [CrossRef]
58. Agostini, I.; Ciuffi, B.; Gallorini, R.; Rizzo, A.M.; Chiaramonti, D.; Rosi, L. Recovery of Terephthalic Acid from Densified Post-consumer Plastic Mix by HTL Process. *Molecules* **2022**, *27*, 7112. [CrossRef]
59. Shafaei, A.; Nikazar, M.; Arami, M. Photocatalytic degradation of terephthalic acid using titania and zinc oxide photocatalysts: Comparative study. *Desalination* **2010**, *252*, 8–16. [CrossRef]
60. Mahmoodi, N.M.; Arami, M. Bulk phase degradation of Acid Red 14 by nanophotocatalysis using immobilized titanium(IV) oxide nanoparticles. *J. Photochem. Photobiol. A Chem.* **2006**, *182*, 60–66. [CrossRef]
61. Miwa, T.; Kaneco, S.; Katsumata, H.; Suzuki, T.; Ohta, K.; Chand Verma, S.; Sugihara, K. Photocatalytic hydrogen production from aqueous methanol solution with $CuO/Al_2O_3/TiO_2$ nanocomposite. *Int. J. Hydrog. Energy* **2010**, *35*, 6554–6560. [CrossRef]
62. Ali, I.; Suhail, M.; Alothman, Z.A.; Alwarthan, A. Recent advances in syntheses, properties and applications of TiO_2 nanostructures. *RSC Adv.* **2018**, *8*, 30125–30147. [CrossRef]
63. Sotiles, A.R.; Barbosa, L.V.; Vedovato, Y.P.; Wypych, F.; de Faria, E.H. Effect of Zn_2Cr layered double hydroxide on photocatalytic hydroxylation of terephthalic acid and photodegradation of sodium diclofenac. *Catal. Today* **2023**, *423*, 114287. [CrossRef]
64. Tawfik, M.; Eskander, S. Recycling of Polyethylene Terephthalate Plastic Wastes based on unsaturated Diol. *KGK Rubberpoint* **2015**, *68*, 21–27.
65. Kulkarni, R.M.; Patwardhan, N.S.; Iyer, P.B.; Bharadwaj, T.D. A review on microbial bioremediation of polyethylene terephthalate microplastics. *Environ. Qual. Manag.* **2024**, *34*, e22264. [CrossRef]

Disclaimer/Publisher's Note: The statements, opinions and data contained in all publications are solely those of the individual author(s) and contributor(s) and not of MDPI and/or the editor(s). MDPI and/or the editor(s) disclaim responsibility for any injury to people or property resulting from any ideas, methods, instructions or products referred to in the content.